Equivalent circuit modelling of new brushless synchronous alternator

N.L. Brown, L. Haydock, E. Spooner, A. Mebarki and A. Novinschi

Abstract: A new type of brushless synchronous machine has been described in the companion paper 'New brushless synchronous alternator' (Brown, N.L. and Haydock, L.: *IEE Proc., Electr. Power Appl.* 2003, **150,** (6), pp. 629–635.) The machine combines permanent magnet and wound coil excitation to provide a single-stage brushless alternator. The simple construction conceals a difficult magnetic circuit that displays complex interactions between excitation sources in the presence of saturation and leakage fields. A design procedure for such a machine using equivalent circuit models is described and the theoretical results are compared with measured values.

List of symbols

A	Area, m^2
A_m	magnet area, m^2
A_p	pole area, m^2
B	flux density, T
D_1	stator inner diameter, m
D_{mean}	mean diameter of stator, m
D_R	rotor outer diameter, m
D_{SH}	shaft outer diameter, m
F	MMF, A
F_a	armature reaction MMF, A
F_D	direct axis armature MMF, A
F_e	excitation coil MMF, A
F_E	equivalent Thevenin equivalent MMF, A
F_m	magnet MMF, A
F_Q	quadrature axis armature MMF, A
H_m	magnet coercive force, A/m
I	stator current, A, rms
K_w	winding factor including pitch and distribution
L_C	stator core length, m
L_D	rotor disk length, m
L_{DS}	rotor disk to stator length, m
L_{gap}	airgap length, m
L_m	magnet length, m
L_{SH}	shaft length, m
N_{ph}	phase turns
p	number of pole pairs
R_1	inner radius of magnet, m
R_2	outer radius of magnet, m
S_E	equivalent Thevenin source reluctance
S_{l1}	back of rotor disk leakage reluctance, A/Wb
S_{l2}	rotor disk to disk edge leakage reluctance, A/Wb
S_{l3}	rotor disk edge to stator edge leakage reluctance, A/Wb
S_{l4}	shaft leakage reluctance, A/Wb
S_{l5}	rotor disk to stator leakage reluctance, A/Wb
S_{leak}	leakage reluctance, A/Wb
S_m	magnet reluctance including airgap, A/Wb
S_{mag}	magnet reluctance, A/Wb
S_p	steel pole reluctance including airgap, A/Wb
S_{shaft}	shaft reluctance, A/Wb
α	pole arc to pitch ratio
λ	flux linkage, Wb
μ_0	permeability of free space, H/m
μ_{rec}	magnet recoil permeability, H/m
ψ	angular displacement between load current and airgap emf, rads

IEE Proceedings online no. 20045040

doi:10.1049/ip-epa:20045040

Paper first received 28th May 2004 and in final revised form 7th December 2004. Originally published online: 15th April 2005

N.L. Brown, L. Haydock, A. Mebarki and A. Novinschi are with Newage AVKSEG-Engineering, Barnack Road, Stamford PE9 2NB, UK

E. Spooner is with Evolving Generation Ltd, Unit 1, Crook Business Centre, Crook, Co. Durham DL15 8QX, UK

E-mail: neil.l.brown@newage-avkseg.com

1 Introduction

New high energy permanent magnet materials have inspired the development of efficient, compact, brushless synchronous machines. However, the absence of any means of excitation control to maintain a regulated output voltage under varying load conditions prevents their use in mainstream generator applications. The Haydock–Brown (HB) machine [1–4] offers an efficient and compact solution for small-scale fixed-speed engine-driven generator applications. The concept uses permanent magnets combined with a field winding attached to the stator to provide the desired excitation control in a single machine.

While similar concepts combining PM and field coil excitation have been researched in recent years [5–7], the HB machine is a new invention and the reader is referred to the companion paper [1] for a full appraisal of it. This paper provides a deeper insight into the modelling aspects and compares theoretical with measured results.

Figure 1 is a schematic diagram of the machine in a four-pole arrangement. The rotor consists of two discs mounted on a common shaft and is entirely ferromagnetic. Each disc carries a set of alternate north and south poles directed axially toward the stator. On one disc the two north poles are permanent magnets and the two south poles are steel. The north poles are located opposite the north poles of the second disc, however, the north poles of the second disc are

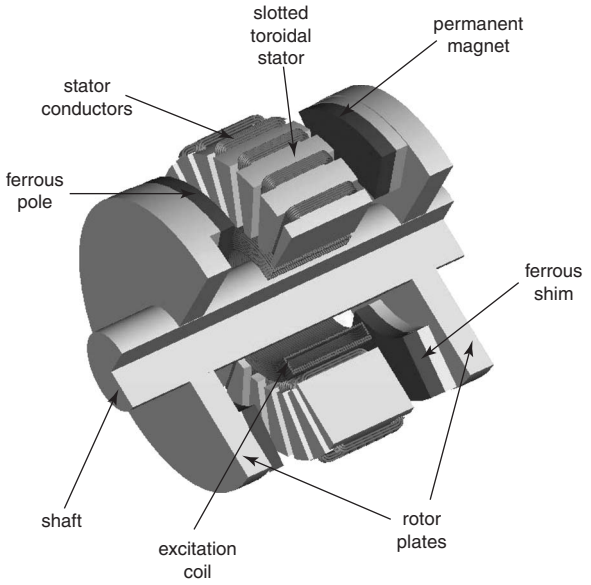

Fig. 1 *Machine structure*

steel and the south poles are permanent magnets. Excitation for the steel south poles of the first disc and north poles of the second is provided by a single coil surrounding the shaft and fixed to the stator. The stator winding comprises of a set of coils each occupying a slot on each of the two faces. The stator resembles that of the TORUS [8] machine, but unlike the TORUS machine it uses a winding in slots.

2 Modelling

A lumped-parameter magnetic equivalent circuit for the machine with armature reaction in the *D*-axis is given in Fig. 2. The magnet is represented by an MMF source F_m in series with a reluctance that includes the airgap and magnet, S_m. The steel poles are represented by the reluctance of the air over the pole arc, S_p. The machine has four poles, hence with two rotors the equivalent circuit includes four magnet poles and four steel poles. The stator core is assumed to be infinitely permeable and so has zero reluctance. The effect of load current in the armature winding is represented by the set of armature reaction MMFs, F_a. A branch representing the shaft with reluctance S_{shaft} and the field winding MMF F_e and a second branch representing the combined leakage paths, S_{leak}, in the space surrounding the machine are shown in parallel with the main part of the equivalent circuit.

All magnetic paths other than in the shaft have been assumed to be linear to simplify the modelling process. The circuit does not include the stator leakage paths but does include the leakage paths that carry flux driven by the excitation coil. The latter is essential for calculating the total shaft flux and, since saturation is a prominent concern, the main and leakage fluxes must be computed together. The stator leakage flux can be calculated separately because it does not pass through any regions liable to saturation.

It should be noted that certain parameters in the equivalent circuit of Fig. 2, such as S_{leak}, F_a, S_{shaft} and F_e are split into two parts to create a central node. This is used later to reduce the circuit complexity by symmetry. For the same reason, three further potentials, labelled 'core potential *A*', 'core potential *B*' and 'core potential $-B$' are specifically identified.

2.1 Equivalent circuit parameters

2.1.1 Steel poles: Flux driven by the permanent magnets and the excitation coil passes across the airgap with a uniform distribution apart from fringe effects near the edges of the pole and the edges of teeth. The usual simple expression for reluctance applies

$$S_p = L_{gap}/(\mu_0 A_p) \tag{1}$$

An adjustment was applied to the area to allow for fringe fields by including a strip around the edge of the pole equal in width to the airgap length. The path length was also increased using the Carter [9] coefficients to account for stator slotting.

2.1.2 Permanent magnet poles: Sintered neodymium–iron–boron magnets are used. The material has a linear second quadrant demagnetisation characteristic with slope typically $1.05 \times \mu_0$. Each magnet was therefore represented in the usual way by its reluctance, (2), in series with an MMF source, (3)

$$S_{mag} = L_m/(\mu_0 \mu_{rec} A_m) \tag{2}$$

$$F_m = H_m L_m \tag{3}$$

where

$$A_m = \alpha\pi\left(R_2^2 - R_1^2\right)/2p \tag{4}$$

It should be noted the equivalent circuit of Fig. 2 uses a magnet reluctance S_m, which includes S_{mag} from (2) and the reluctance of the airgap under the magnet pole.

2.1.3 Stator D-axis MMF: The armature winding is designed to create an MMF distribution that approximates

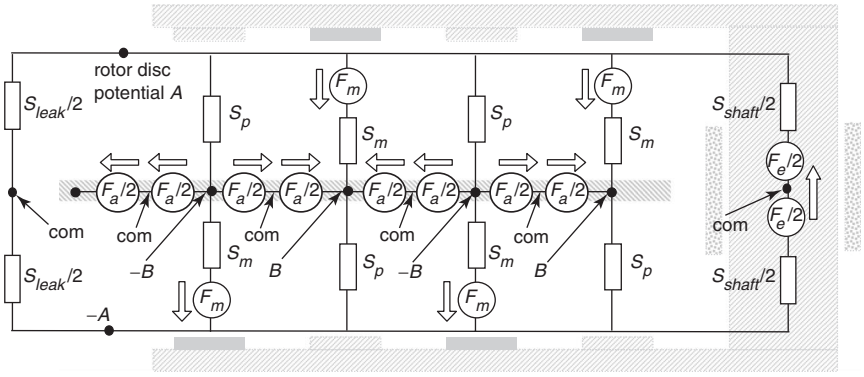

Fig. 2 *Magnetic equivalent circuit with armature current in the D-axis*
Physical parts shown in relationship

a sinewave and the resulting armature reaction flux is distributed likewise. For the magnetic equivalent circuit of Fig. 2 we require an equivalent single value for the armature reaction MMF that yields the same result. We consider the steel poles for simplicity but the same result would be obtained by considering the magnet poles.

$$flux\ density, B = \frac{\hat{F}}{L_{gap}}\mu_0 \cos(p\theta) \tag{5}$$

where

$$\hat{F} = \sqrt{2} I N_{ph} \frac{3}{2}\frac{K_w}{2p}\frac{4}{\pi} \tag{6}$$

and L_{gap} is adjusted by the Carter factor to allow for the stator slotting.

The elemental area, dA, is

$$dA = (R_2 - R_1)\frac{(R_1 + R_2)}{2}\, d\theta \tag{7}$$

where R_1 and R_2 are modified to include the fringe zone around the pole.

The total D-axis flux, ϕ_D per pole is found by integrating over the pole arc with the peak flux density occurring at the centre of the pole (Fig. 3a).

$$\begin{aligned}\phi_D &= \mu_0 \frac{\hat{F}}{L_{gap}}\frac{\left(R_2^2 - R_1^2\right)}{2}\int_{-\alpha\pi/2p}^{\alpha\pi/2p} \cos(p\theta)d\theta \\ &= \frac{\mu_0 \hat{F}(R_2^2 - R_1^2)}{pL_{gap}}\sin\left(\frac{\alpha\pi}{2}\right)\end{aligned} \tag{8}$$

where the pole arc over pole pitch α has been modified to include the flux fringe at the edge of the pole.

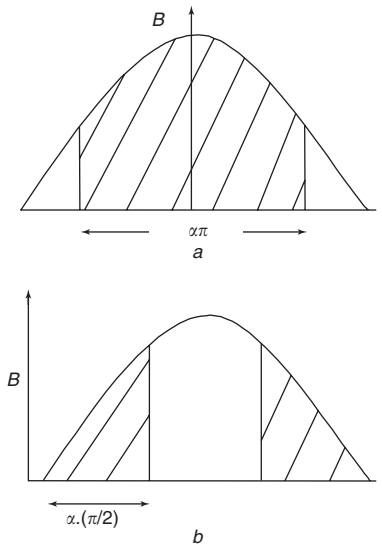

Fig. 3 *Calculation of D- and Q-axis flux*
a Direct axis flux
b Quadrature axis flux

Now, consider Fig. 2 for the case where the excitation MMF and the magnet MMF are set to zero, then the circuit is clearly symmetrical about the nodes labelled 'com' and the flux passing through each of the reluctances S_p is

$$\phi_D = \frac{F_a}{2S_p} \tag{9}$$

The pole reluctance is given by (1) using the modifications to R_1 etc. for fringe fields.

$$S_p = \frac{L_{gap}}{\mu_0 \alpha\pi(R_2^2 - R_1^2)/2p} \tag{10}$$

so from (8)–(10) the effective value for F_a is

$$F_a = 2\hat{F}\frac{\sin(\alpha(\pi/2))}{\alpha(\pi/2)} \tag{11}$$

In general, different pole arc widths could be employed for the steel and magnet poles and so different values of α would apply for the armature MMF applied to the two-pole types. In such cases a more complex connection arrangement should be adopted in the region of the nodes labelled B and $-B$. In practice, the two pole arcs will be similar if not identical and any small discrepancy is accepted in the context of a lumped-parameter equivalent circuit approximation to the full electromagnetic system. The majority of the armature reaction flux passes through the steel poles and the value of α for these is the appropriate one to adopt if there is any difference.

2.1.4 Stator Q-axis MMF:

F_Q is not needed in the analysis of the equivalent circuit of Fig. 2 which uses only the D-axis component of the armature MMF but it is required in subsequent analysis to find the q-axis reactance of the machine and is included here for completeness. The armature MMF is aligned with its peak value between the poles, Fig. 3b, so the armature reaction flux density is greatest at the ends of the poles and zero at the centre. The flux per pole carried by a pair of adjacent steel poles is

$$\phi = \mu_0 \frac{\hat{F}}{L_{gap}}\frac{\left(R_2^2 - R_1^2\right)}{2} 2\int_0^{\alpha.\pi/2p} \sin(p\theta)d\theta \tag{12}$$

giving

$$F_Q = \hat{F}\frac{\{1 - \cos(\alpha(\pi/2))\}}{\alpha(\pi/2)} \tag{13}$$

In addition, a significant amount of Q-axis flux passes in the interpolar space and in the permanent magnet pole where the effective airgap is equal to the iron–iron space.

The reluctance of the interpolar space has a similar form to (1). The effective MMF required to find the Q-axis flux in the interpolar space is the same as (11) using the Q-axis armature current and replacing α by $(1-\alpha)$.

2.1.5 Leakage paths:

The complex 3D geometry and homopolar MMF make flux leakage a major design concern. Several distinct paths have been combined in parallel to form the single reluctance, S_{leak} shown in the magnetic equivalent circuit of Fig. 2. Figure 4 identifies the principal leakage paths and their separate reluctance values which have been estimated as follows.

S_{l1} refers to leakage from the outer faces of the rotor discs and was derived by scaling from a 3D finite-element study for a simple steel cylinder of 1 m diameter, 0.2 m length excited by a solenoid coil.

$$S_{l1} = \frac{3 \times 10^6}{D_R} \tag{14}$$

S_{l2} refers to the leakage between the edges of the two rotor discs. This was estimated by means of a simple analytical formula based on the fact that an open magnetic circuit over a cylindrical surface carries a total flux similar to that carried by a uniform field in an airgap equal to (pole-pitch)/π.

$$S_{l2} = \frac{L_{SH} + L_D}{\pi(D_R \pi L_D)\mu_0} \tag{15}$$

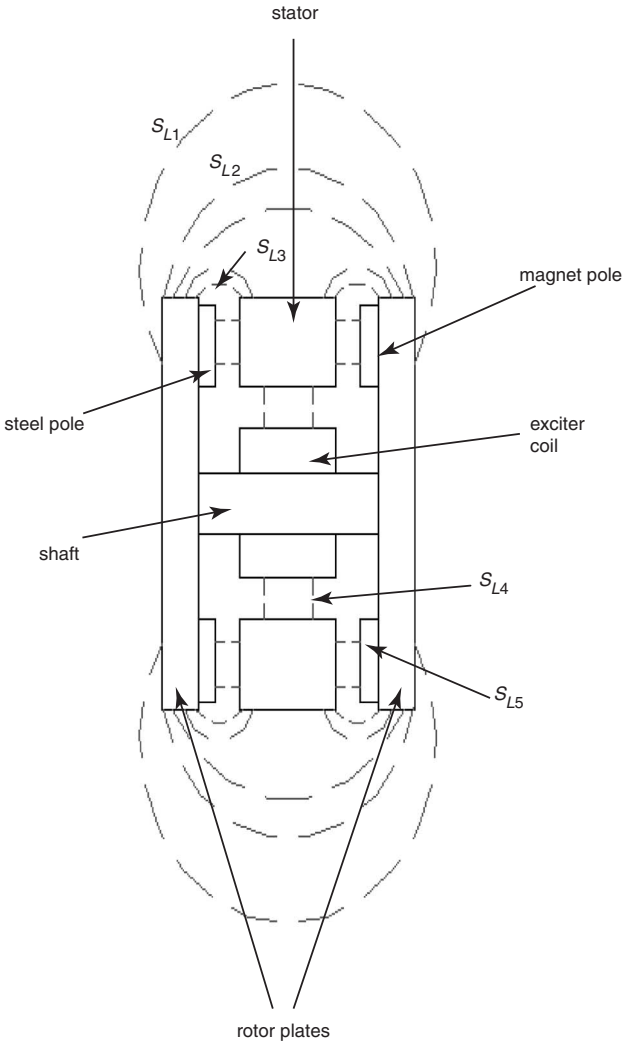

Fig. 4 *Leakage flux within machine*

S_{l3} refers to leakage between the edge of each rotor disc and the edge of the stator core. It is estimated in the same manner as S_{l2}.

$$S_{l3} = \frac{L_{DS} + L_D}{\pi(D_R \pi L_D)\mu_0} \tag{16}$$

S_{l4} refers to leakage flux passing between the shaft and the inside surface of the stator. This component was estimated in a very approximate way by assuming the flux to follow purely radial paths and neglecting curvature and the fringe flux around the ends of the coil. This calculation resembles the calculation of leakage flux due to current in an armature slot.

$$S_{l4} = \frac{(D_1 - D_{SH})/2}{\mu_0 \pi \dfrac{(D_1 + D_{SH})}{2}\left(L_{DS} + \dfrac{L_C}{2 \times 3}\right)} \tag{17}$$

S_{l5} refers to the flux passing axially from rotor disk to stator in the regions between poles. In a P-pole machine there are $P/2$ magnet and $P/2$ iron poles on each disc thus

$$S_{l5} = \frac{L_{DS}}{\mu_0\left\{\dfrac{\pi}{4}\left(D_R^2 - D_{SH}^2\right) - pA_m - pA_p\right\}} \tag{18}$$

The various leakage paths are combined in parallel to form the single leakage path shown in the equivalent circuit. The regions corresponding to S_{l2} and S_{l3} overlap and so the parallel combination overestimates the total leakage.

$$S_{leak} = \frac{1}{\left(\dfrac{1}{S_{l1}} + \dfrac{1}{S_{l2}} + \dfrac{1}{2S_{l3}} + \dfrac{1}{2S_{l4}} + \dfrac{1}{2S_{l5}}\right)} \tag{19}$$

2.1.6 Nonlinear shaft model: The shaft is the principal bottleneck in the magnetic circuit. The transition from no-load to full-load operation reverses the shaft flux and saturation can occur in either case unless an adequate cross-section is provided.

Feeding current to the excitation coil, with no current in the stator, first takes the shaft out of saturation with little effect on the total armature flux and EMF. Increasing excitation current reduces then reverses the shaft flux and eventually causes saturation in the opposite sense. Clearly a nonlinear model of the shaft is required. This should take account of any ventilation holes in the shaft and flux concentrations at the junction between the shaft and the disc. A lumped parameter model was developed based upon the geometry of the shaft and the geometry of the junction between the shaft and disc. The accuracy of this model was verified using 3D finite-element analysis. The material characteristic of the low carbon steel used in the shaft (EN1A) was measured and by means of least-square curve fitting an analytical function, (20), was found that gave very close fit as shown in Fig. 5. The RMS error in H is 42 A/m, which is probably considerably less than the differences in practice between manufactured pieces. A polynomial function, containing only odd powers, is guaranteed to display the required symmetry about the origin.

$$\begin{aligned} H = {} & 966B + 586B^3 \\ & + 0.119B^{19} - 0.000462B^{25} \end{aligned} \tag{20}$$

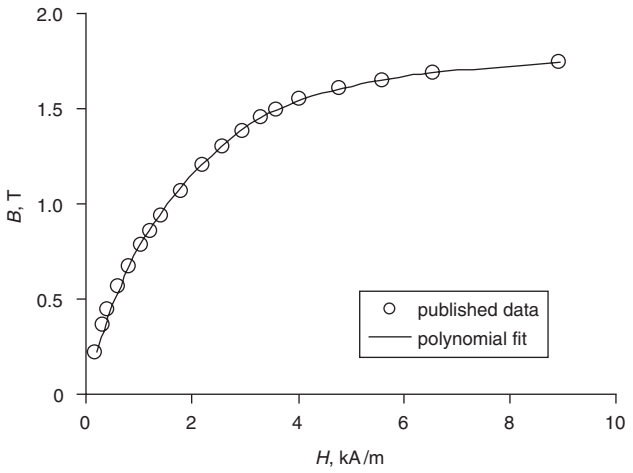

Fig. 5 *Analytical model result for iron B-H characteristic*

2.2 D-axis magnetic circuit analysis

The equivalent circuit of Fig. 2 is nonlinear because the shaft reluctance is nonlinear. A circuit having a single nonlinear element can be analysed by the load line method. First it is necessary to transform the rest of the circuit to a form in which the nonlinear element is fed by a simple Thevenin type source comprising an MMF source in series with a constant reluctance.

The transformation is simplified by recognising that the centre point of each armature branch is at the same potential as the centre point of the shaft so that the circuit

possesses symmetry about this midpoint node and reduces to the form shown in Fig. 6 with two unknown node potentials.

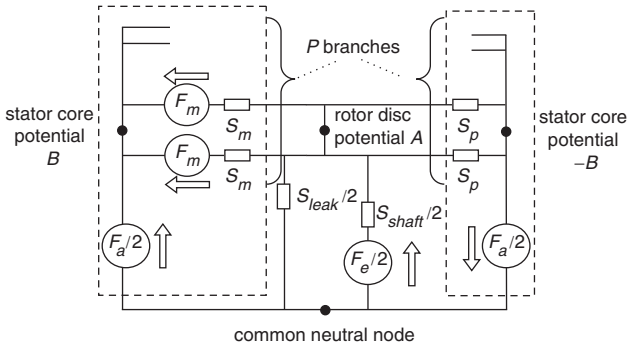

Fig. 6 *Reduced D-axis equivalent circuit*

The reduced circuit of Fig. 6 is further transformed by replacing the two element groups indicated by their Norton equivalent sources to create the circuit shown in Fig. 7.

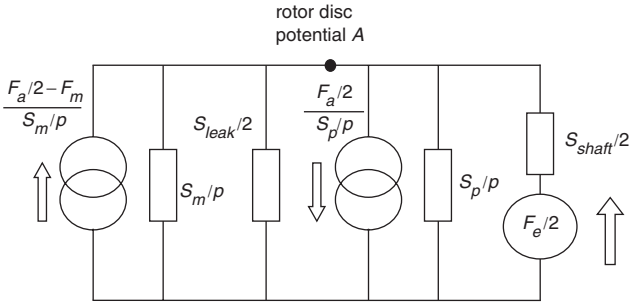

Fig. 7 *Current sourced equivalent circuit*

Finally, the circuit is further reduced to the nonlinear reluctance of the shaft driven by a Thevenin source, Fig. 8, where

$$S_E = \frac{1}{\frac{1}{S_m/p} + \frac{1}{S_{leak}/2} + \frac{1}{S_p/p}} \tag{21}$$

$$F_E = S_E\left\{\frac{F_a/2 - F_m}{S_m/p} - \frac{F_a/2}{S_p/p}\right\} - \frac{F_e}{2} \tag{22}$$

Figure 9 shows the load line approach to the solution of the nonlinear circuit. The flux / MMF characteristic of the shaft

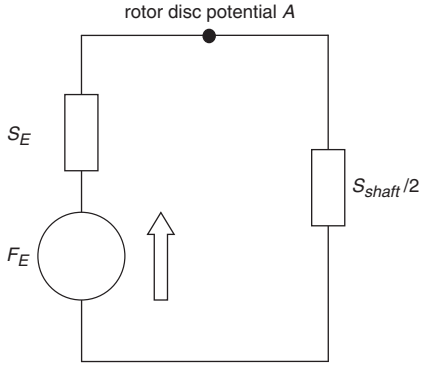

Fig. 8 *Reduced Thevenin equivalent circuit*

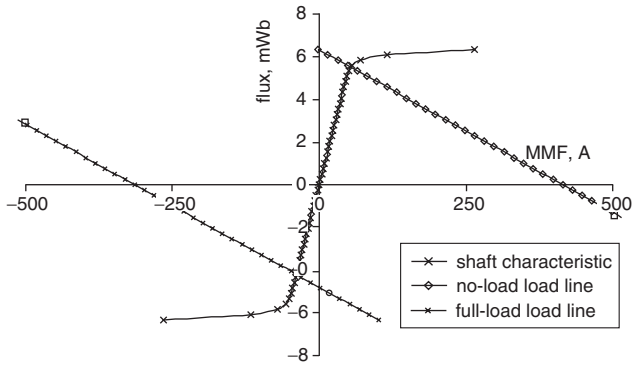

Fig. 9 *Load line calculation of rotor disc potential*

is plotted together with the linear characteristic of the Thevenin source and the intersection gives the shaft flux and MMF. Knowledge of the rotor disc potential then allows all the fluxes in the original circuit of Fig. 2 to be calculated.

The no-load voltage may be calculated by setting F_a to zero and computing F_1 and S_1, then using the Thevenin equivalent circuit in Fig. 8 to calculate the disc potential A and the subsequent flux within the original circuit of Fig. 2. The case of full-load *D*-axis current gives the maximum operational shaft flux from which the requisite shaft diameter can be derived. The same case also gives the armature full-load flux linkage. Adjusting the field current to restore the flux linkage to the no-load value leads to the required coil excitation.

2.3 Allowance for varying power factor loads

So far the analysis has only considered operation for zero power factor loads when the armature flux is in the *D*-axis. It has been recognised [1] that armature *Q*-axis flux does not pass along the shaft. Therefore unity power factor loads do not influence the shaft flux. For the calculation of shaft flux we therefore need just the *D*-axis component of the armature MMF which can be obtained from the complete armature MMF and the internal power factor. For clarity the internal power factor is defined here as the angular displacement between terminal voltage and load current added to the angular displacement between the terminal voltage and the internal EMF resulting from stator leakage inductance and resistance. The value of F_E for use in Fig. 8 is therefore

$$\begin{aligned} F_E = & F_a \sin\psi \frac{S_E}{2}\left\{\frac{1}{S_m/p} - \frac{1}{S_p/p}\right\} \\ & - F_m \frac{S_E/2}{S_p/p} - \frac{F_e}{2} \end{aligned} \tag{23}$$

where, $\cos\psi$ is the internal power factor, which corresponds to the real and reactive power flow across the airgap.

2.4 Stator leakage

For the purpose of predicting the machine performance, several flux paths were considered that carry flux driven by stator current and are not included in Fig. 2. These are grouped together as stator leakage and include the familiar forms of leakage as well as others specific to this special machine configuration.

- slot leakage
- end winding leakage, at both the inner and outer edges of the stator. Note that the shaft has a significant impact on the inner leakage field

• airgap armature leakage, caused by the proximity of the rotor discs

• *D*- and *Q*-axis leakage over steel pole, caused by the proximity of the pole to the armature

The last component in particular presents a difficulty, common in lumped parameter analysis, whereby it is unclear how to allocate components to leakage or magnetising branches of the equivalent circuit, because this flux component shares parts of its path with the *Q*-axis flux discussed earlier. Another difficulty arises because this particular component of leakage flux is sensitive to the internal power factor. For simplicity, its value was calculated using the terminal power factor.

In the design procedure, the following calculation sequence was adopted:

(1) a target voltage, load current and power factor is specified and the leakage inductance calculated

(2) from the leakage inductance, stator resistance and load power factor an internal power factor is established

(3) using the internal power factor the armature excitation F_a is calculated and using the magnetic equivalent circuit the EMF is calculated

(4) the stator leakage reactance and stator resistance is used in conjunction with the load current to obtain the terminal voltage from the internal EMF calculated in (3)

3 Test and validation

A number of tests were carried out and comparisons were made with predictions derived from the magnetic equivalent circuit model.

3.1 No-load magnetisation curve without magnets

The machine was first assembled without magnets so that the performance of the excitation coil alone could be assessed. Figure 10 shows the corresponding no-load magnetisation characteristic obtained by monitoring the output voltage and varying the DC current in the excitation coil. The measured and calculated values are seen to follow a similar trend demonstrating that the shaft model is acceptable. The *BH* characteristic used in the model was measured from a sample of material of the type used in the shaft and an analytic function of the form of (20) was fitted to the data. Apart from the shaft, the magnetic circuit operates with quite low flux density and is expected to be magnetically linear. The difference between measured and calculated values (13.9% at 0.5 A and 5.4% at 4 A) can be attributed largely to errors in the airgap and leakage field reluctances, as indicated by the different airgap lines shown dotted in Fig. 10.

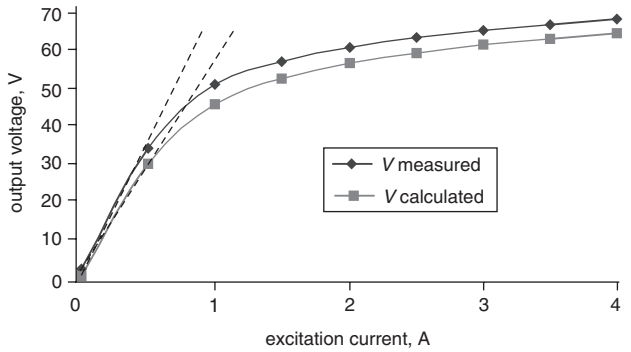

Fig. 10 *No-load magnetisation curve without magnets*

3.2 Short-circuit curve without magnets

Figure 11 gives the short-circuit curve for the machine without any magnets. Here the output of the machine was shorted through a power analyser and the output current with respect to excitation current recorded.

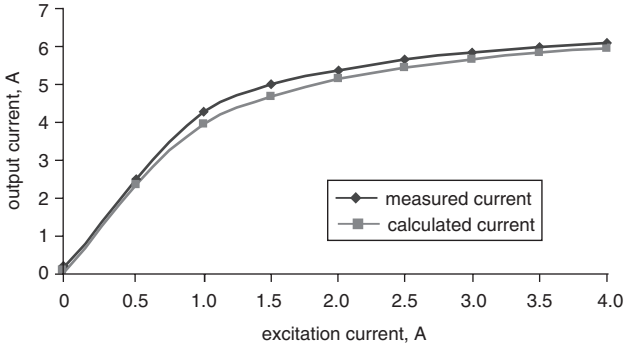

Fig. 11 *Short-circuit curve without magnets*

For low and high excitation currents there is very good agreement between measured and calculated. This suggests the stator armature leakage is well represented in the equivalent circuit. There is a maximum error of 8.3% at 1 A but it has already been identified that the airgap and leakage fields are not quite correct. For an excitation level of 4 A the error reduces to 2.4%. The calculated level of current being lower than measured is consistent with what was observed for the no-load case, Fig. 10. The low levels of short-circuit current ensured thermal effects did not mask the measured results. It should be noted that unlike conventional synchronous machines, which display a linear short-circuit characteristic, the high degree of field leakage and the marked tendency for the shaft to saturate produce a saturating characteristic in this machine.

3.3 Open circuit voltage with magnets

With the magnets present, the excitation current was varied from −4 A to +4 A and the no-load output voltage was monitored. The measured and calculated voltage shown in Fig. 12 are extraordinarily close considering the imperfections in the magnetic circuit. For example with no allowance made for pole, teeth or core-back in the magnetic circuit, a measured voltage lower than calculated was

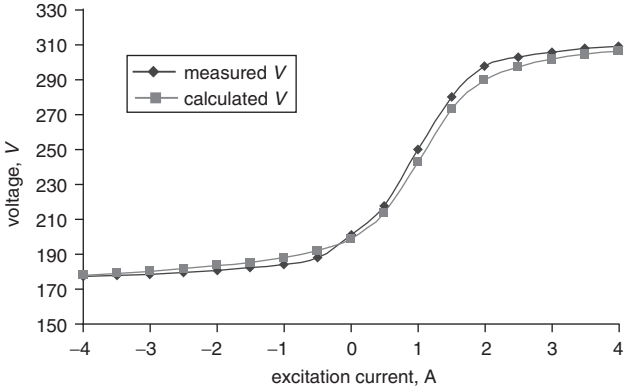

Fig. 12 *No-load voltage with magnets*

expected. Magnets also have variable performance. Therefore the close correlation is due to a combination of second-order effects such as those described above compensating for some of the basic assumptions in the model. Points to note are that the calculated voltage as a result of the excitation current is still underestimated. For the −4 A point the coil and magnets drive flux in the same direction along the shaft, which is therefore heavily saturated masking uncertainties in the separate flux contributions.

This open-circuit voltage, Fig. 12, was taken before the machine had ever operated under load. After various loads were applied the no-load voltage due to the magnets acting alone tended to stabilise at a slightly lower level around 194 V compared with an initial value of 201 V. This phenomenon has been observed before in permanent magnet machines and should be recognised as a general issue with permanent magnet machines. Despite their excellent properties, rare-earth magnets are subject to a small reduction in magnetisation when stabilised particularly if used to overcome a high reverse field. Further slight variations about the stabilised voltage were observed from day to day.

Comparing Figs. 10 and 12 reveals the effect of the field current is greater when magnets are present. For example, a 4 A field current applied in the absence of magnets causes an EMF of just under 70 V to be induced, Fig. 10. At 0 A in Fig. 12 the induced voltage is 200 V and is a result of magnets only. Further inspection of Fig. 12 indicates for a 4 A current the EMF increases by around 110 V when used in conjunction with magnets. The reason for the EMF increasing by 110 V rather than 70 V is a consequence of the nonlinear behaviour of the shaft. Magnets produce flux in one direction and the current first reduces this to zero, then creates shaft flux in the opposite direction. The available range, if leakage and magnetic loading in the shaft is ignored, could be doubled by the presence of magnets if the machine is designed so that the magnets alone just saturate the shaft.

3.4 Zero power factor load

A set of load tests at zero power factor was carried out. The current is mostly aligned with the *D*-axis and so the circuit of Fig. 2 is an accurate reflection of the conditions in the machine. Figure 13 displays the recorded voltage as load current was varied, for several fixed excitation current settings. The measured no-load voltage was slightly lower than calculated but as load current increased the measured voltage was higher. This observation suggests the calculated internal impedance was slightly higher than actually present.

The model did not include an allowance for the increased magnet temperature due to the proximity of the stator as load current was drawn. Therefore the calculated results should have been slightly higher than measured. This discrepancy is likely to be the result of the calculated leakage reactance being a little higher than reality.

Overall there was very good agreement between measured and calculated performance, indicating that the parameters representing the permanent magnets, steel poles, nonlinear shaft and the *D*-axis armature MMF are acceptably accurate.

3.5 Unity and 0.8 power factor loading

Tests were repeated but this time with a 0.8 power factor load. The 0.8 power factor was chosen, as most stand-alone generators are sold commercially at a 0.8 power factor rating. Clearly from Fig. 14 the model has represented the

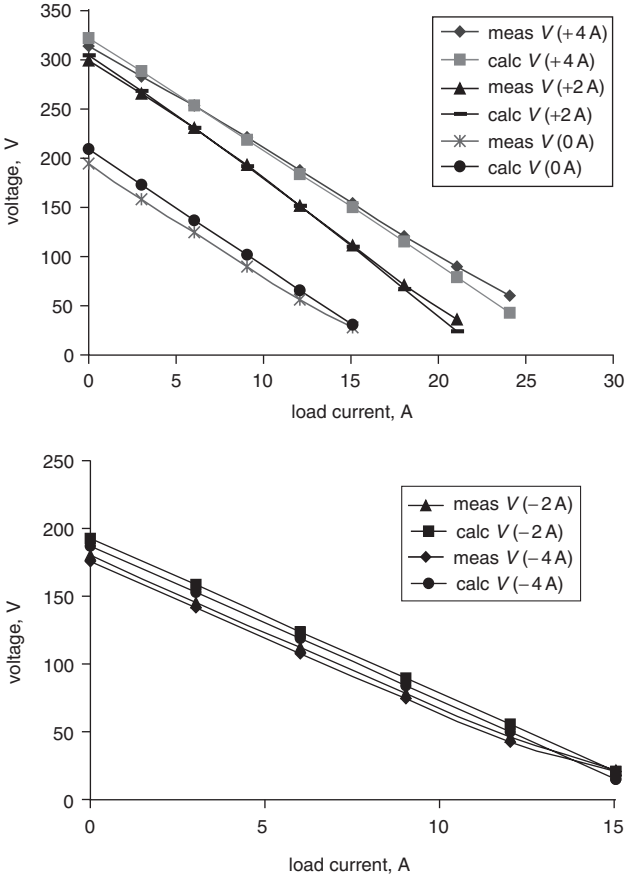

Fig. 13 *Zero power factor loading with fixed excitation*

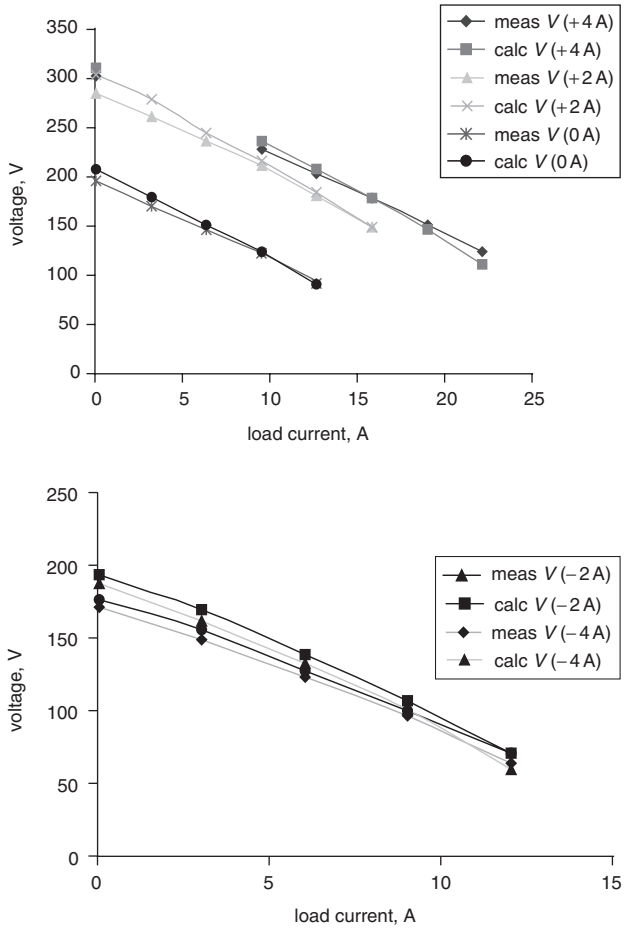

Fig. 14 *0.8 power factor loading for fixed excitation*

machine very well. As with the zero power factor case the predicted no-load voltage was higher but the model had slightly higher internal impedance.

3.6 Unity power factor loading

All tests have been performed with a diesel engine as the prime mover. With finite power available from the engine there was some difficulty regulating the speed as load was applied and the calculated and measured results suffer from slight frequency variations. For the +4 A case the tests had to be performed by first loading the generator to limit the amount of power drawn from the engine, hence the incomplete set of results.

Other than for the 0 A excitation case, all the calculated results were greater than measured. This discrepancy is likely to be due to how the *Q*-axis flux is modelled. Modelling in the *Q*-axis is more difficult than the *D*-axis with flux paths not as well defined. Bearing in mind that the lower power factor load is more demanding and will establish the rating of the machine, the unity power factor readings are acceptably close and clearly follow the trend of the measured result. For the 0 A case it is not clear why this has not followed a similar trend to the other results. However, maintaining engine speed was difficult and experimental error will be present.

3.7 Thermal tests

Cooling this machine was a concern as the shaft cross-sectional area required for magnetic purposes restricts the available cross-sectional area for admitting cooling air, and the presence of the excitation coil obstructs airflow inside the machine leading to a severe design conflict in the inner region. It was decided that the prototype should be designed for the highest electromagnetic torque possible and to accept the compromised thermal performance (Fig. 15).

An important observation during testing was that as the machine was loaded the magnet performance tended to degrade with temperature, placing more demand on the excitation system. As a direct result of shaft saturation, when the machine was loaded with the terminal voltage maintained at a constant level, it was easy to overexcite the coil, as an increase in excitation did not give a proportional increase in flux. This, coupled with the increasing stator resistance with temperature, puts further demands on the excitation system. For these reasons the steady-state thermal capability of the machine is quite moderate.

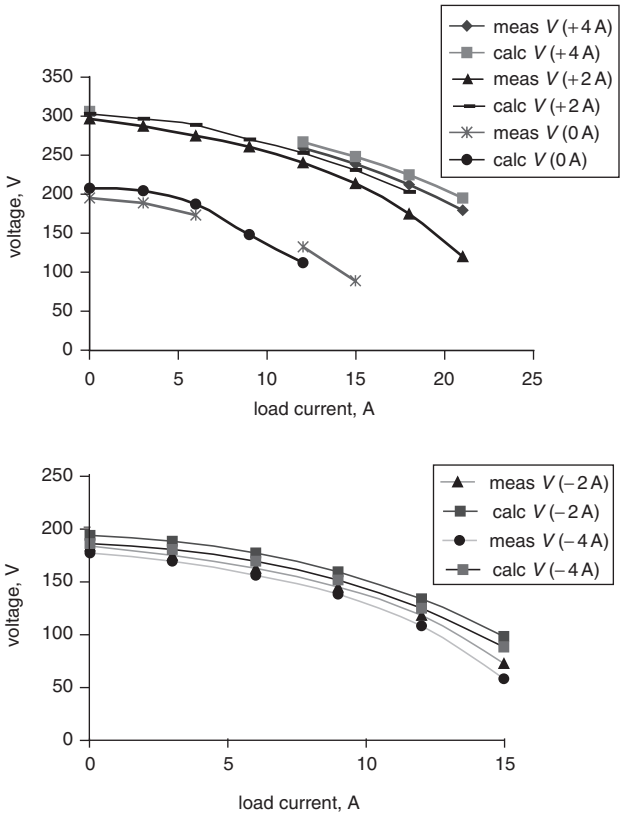

Fig. 15 *Unity power factor loading for fixed excitation*

Table 1 provides details of the temperature of the machine after a 3 hour heat run when loaded with 6 kVA at 0.8 power factor. At shut down the temperature rise by resistance of the stator windings was recorded as 67 K. Clearly the excitation current has increased from 2.64 A cold to 3.1 A hot. A load of 6.5 kVA at 0.8 power factor was tried but the excitation coil went into a thermal runaway condition.

Table 1: 6 kVA 0.8 power factor heat run

Time	V	A	kW	kVA	Excitation A	Excit. coil temp., °C	Air in, °C	Air out, °C
09:30	200.6	–	–	–	0.320	28	9.9	21.8
09:35	202.9	9.99	–	6.079	2.364	38	11.3	25.3
09:45	203.4	10.09	–	6.179	2.437	46.8	12.8	29.3
10:00	203.9	10.39	4.940	6.349	2.6411	57	13.8	33.3
10:15	204.7	10.55	5.226	6.461	3.4391	81.2	12.5	38.1
10:30	203.1	10.42	5.141	6.343	3.257	94.4	15.8	42.5
10:45	202.1	10.36	5.085	6.274	3.2161	97	16.4	45.8
11:00	201.2	10.31	5.043	6.220	3.180	100.6	19.8	42.5
11:15	200.7	10.23	5.017	6.187	3.1666	100.1	15.6	48.8
11:30	200.2	10.25	4.987	6.152	3.1466	102.2	16.3	49.1
11:45	200.1	10.25	4.983	6.144	3.1364	105.2	18.4	51
12:00	199.7	10.23	4.957	6.122	3.1216	105.3	18.3	50.9
12:15	199.4	10.21	4.948	6.101	3.1143	105.6	17.5	50.9
12:30	199.3	10.21	4.945	6.097	3.1132	103.9	16.1	51.9

4 Conclusions

With the electromagnetic limit set by the shaft dominating the design, all the analysis has assumed linearity in the pole, tooth and core back. Saturation effects in these parts need to be considered in future development. Several aspects of the design offer considerable scope for optimisation such as slot profile, magnet and steel pole shape. However, the lumped-parameter equivalent circuit model has delivered excellent results especially for cases where loading is predominantly in the *D*-axis.

Some refinement may still be required in the *Q*-axis but it is not thought essential at this stage in the development.

While the design process is difficult, once experience of prototype machines has been gained and relative comparisons made in FEA, designs can be readily adjusted with a degree of confidence.

5 Acknowledgments

The authors acknowledge the permission of Newage-AVK-SEG to publish this paper and the invaluable support of the technical and manufacturing staff within the engineering department of the company, in particular S. Ruffles, S. Walton and S. Coulson.

6 References

1 Brown, N.L., and Haydock, L.: 'New brushless synchronous alternator', *IEE Proc., Electr. Power Appl.*, 2003, **150**, (6), pp. 629–635
2 Brown, N.L., Haydock, L., Spooner, E., Mebarki, A., and Novinschi, A.: 'Introduction to a novel axial flux PM synchronous machine with excitation control'. Proc. IEE PEMD, Edinburgh, UK, 2004, pp. 868–872
3 Mebarki, A., Spooner, E., Brown, N.L., Novinschi, A., and Haydock, L.: 'A non-linear model of a novel axial flux permanent magnet machine with excitation control'. Proc. IEE PEMD, Edinburgh, UK, 2004, pp. 793–798
4 Novinschi, A., Brown, N.L., Spooner, E., Mebarki, A., and Haydock, L.: 'Finite element analysis of a novel axial flux PM synchronous machine with excitation control'. Proc IEE PEMD, Edinburgh, UK, 2004, pp. 420–425
5 Eastham, J.F., Evans, P.D., Coles, P.C., and Ibrahim, M.: 'Double disc alternators with hybrid excitation', *IEEE Trans. Magn.*, 1992, **28**, (5), pp. 3039–3041
6 'Direct control of air gap flux in permanent magnet machines', US Patent No 6057622, May 2000
7 Aydin, M., Huang, S., and Lipo, T.A.: 'A new axial flux surface mounted permanent magnet machine capable of field control'. Proc. IEEE Industry Applications Society Annual Meeting, 2002, pp. 1250–1257
8 Rash, N.M., Spooner, E., and Howe, D.: 'A permanent magnet alternator for use as an electrodynamic railway brake'. Proc. IEE Conf. Electrical machines, design and applications, 1985
9 Carter, F.W.: 'Note on airgap and interpolar induction', *IEE.*, **29**, pp. 925–933